Article

Double-String Battery System with Reconfigurable Cell Topology Operated as a Fast Charging Station for Electric Vehicles [†]

Jan Engelhardt [1] , **Jan Martin Zepter** [1] , **Tatiana Gabderakhmanova** [1] , **Gunnar Rohde** [2] and **Mattia Marinelli** [1,*]

1   Department of Electrical Engineering, Risø Campus, Technical University of Denmark,
    4000 Roskilde, Denmark; janen@elektro.dtu.dk (J.E.); jmwze@elektro.dtu.dk (J.M.Z.);
    tatigab@elektro.dtu.dk (T.G.)
2   Nerve Smart Systems ApS, 4000 Roskilde, Denmark; gunnar@phyfficus.eu
*   Correspondence: matm@elektro.dtu.dk
†   This paper is an extended version of our paper published in the Proceedings of the 2020 55th International
    Universities Power Engineering Conference (UPEC), Turin, Italy, 1–4 September 2020.

Abstract: This paper introduces a novel design of an electric vehicle (EV) fast charging station, consisting of a battery energy storage system (BESS) with reconfigurable cell topology. The BESS comprises two battery strings that decouple the power flow between EV and grid, to enable charging powers above the grid capacity. The reconfigurable design is achieved by equipping the battery cells with semiconductor switches and serves two main purposes. First, it aims at solving cell unbalance issues to increase safety, reliability, and lifetime of the battery. Second, it enables the BESS to actively control the EV charging process by changing its cell configuration in a real-time fashion, making a DC-DC converter redundant. The paper presents a modelling approach that captures the reconfigurable design including the controlling algorithm used for cell engagement. The simulation results show that the BESS is able to fulfil the EV request with sufficient accuracy for most of the fast charging process. However, the switching of cells leads to variations in the charging current that can potentially exceed the tolerance band defined in IEC61851-23. Therefore, complementary measures are suggested to achieve a suitable current control during all phases of the charging process. The estimated BESS efficiency during the EV fast charging process is 93.3%. The losses caused by the reconfigurable design amount to 1.2% of the provided energy. It is demonstrated that the proposed design has a competitive efficiency compared to a battery buffered fast charging station with DC-DC converter.

Keywords: adaptive cell switching; battery balancing; battery management system; battery energy storage system; DC-DC converter; electric vehicle; energy efficiency; fast charging; reconfigurable battery

1. Introduction

The transportation sector is currently experiencing a paradigm shift as gasoline-powered vehicles are being gradually replaced with electric vehicles (EVs). Driven by global ambitions to phase out fossil fuels, the integration of EVs in the electricity network offers the opportunity for a future mobility powered by renewable energy sources such as wind and solar [1].

While the number of EVs has been increasing in recent years, typical concerns of potential costumers remain range anxiety, long charging times, and insufficient charging infrastructure [2,3]. It is therefore expected that an increased deployment of fast charging stations will help to mitigate those concerns and enable the widespread adoption of EVs [3,4]. Yet, EV fast charging processes pose new challenges for the electric grid due to the high peak-load demand [5–7]. Furthermore, the optimal placement of fast chargers is

restricted by the power capacity at the local grid connection point. Upgrading the existing grid infrastructure is costly and may delay the necessary installation of fast chargers [8]. One solution is to equip the fast charger with a battery energy storage system (BESS), which can be integrated in various ways [9–14]. The battery serves as a buffer to decrease the impact of EV charging on the grid. Therefore, the charging station can provide power levels above the grid capacity, making an upgrade of the grid infrastructure redundant.

To provide the required voltage and current levels in practical applications, battery systems reveal a modular and scalable design. Individual battery cells are electrically connected into modules, and several of these battery modules are integrated with required peripheral equipment into strings and complete systems [15]. The topology of a battery system defines how its cells are connected; a N_pN_s-topology indicates that N_p battery cells are connected in parallel while N_s battery cells are serially connected. However, due to production tolerances and temperature gradients during operation, individual battery cells can show different characteristics and deviating ageing processes. These unbalance issues decrease the effective capacity of the whole battery, as charging and discharging processes are limited by the weakest cells [16]. Moreover, cells with a lower average capacity are more likely to be overcharged or overdischarged compared to other cells. This accelerates their ageing process further and increases the already existing unbalance issues. Eventually, faulty cells may cause the entire battery to become nonfunctional, leading to unscheduled down-time of the system. Therefore, sufficient cell balancing techniques are required to improve energy efficiency, reliability, and life span of the battery [17]. A promising solution is to design battery systems with a reconfigurable topology, where the cell connection scheme can be actively changed during operation [18–21]. With this approach all battery cells can be operated according to their individual state which helps to reduce unbalance issues and deviating ageing processes. In contrast to battery systems with fixed topology, faulty cells can be permanently bypassed to avoid down-time as well as unscheduled maintenance. The respective cells can then be replaced during regular maintenance of the battery system. Another advantage is that the battery voltage can be actively controlled by changing the cell configuration. Hence, the battery can be used to directly supply other DC components, as shown in a previous study [22].

In the present work we adopt the concept of a reconfigurable cell topology in a double-string BESS to operate it as a fast charging station. One string is providing charging power to an EV, while the other string is getting recharged through a grid-connected inverter. The reconfigurable design is utilised in two different ways. First, it is used to directly fulfil the EV charging request by adapting the cell configuration in a real-time fashion. Hence, no DC-DC converter is used for controlling the charging process, which saves investment costs and possibly power losses. Second, it is used to balance the cell states during both charging and discharging. By operating all cells according to their individual performance, the battery management can increase safety, reliability, and lifetime of the whole battery system. The main contributions of the work are:

- The paper proposes a novel design of a double-string battery system with reconfigurable cell topology. The BESS is operated as a fast charging station for EVs and serves as a buffer to reduce the impact of charging processes on the grid.
- A modelling approach for this BESS is presented in detail, with particular focus on the reconfigurable design. The model description includes a controlling algorithm that decides on the connection state of each individual cell.
- The model is used to demonstrate how the BESS can control the power transfer to an EV by changing its cell topology in a real-time fashion. The performance of this approach is compared to the requirements defined in charging standard IEC61851-23, and limitations of the technology are discussed.
- The capability of the BESS to maintain balanced cell states is assessed for both charging and discharging processes. In this respect, the losses caused by the reconfigurable design are estimated for both strings.

The rest of this paper is organised as follows. The proposed BESS design is described in Section 2. Section 3 focuses on the modelling approach for BESS, EV, and inverter. It further includes a description of the controlling algorithm that decides on the connection state of each individual cell. The case study is outlined in Section 4. Simulation results are presented in Section 5 and discussed in Section 6. Finally, the main findings and conclusions are summarised in Section 7.

2. System Design

Figure 1 provides an overview of the double-string system considered in the present study. EVs can be plugged in at the charging port which serves as an interface to the BESS. In the shown configuration, String 1 is providing charging power to the connected EV, while String 2 is getting recharged through a grid-connected inverter. In principle, the two strings are switched if the charge level of String 1 drops below a certain threshold. As this case is not part of the present investigation, it is defined that in the following String 1 and String 2 stay connected to their respective component. As indicated in Figure 1, each string consists of 12 modules, while a module contains 27 series-connected cells. The reconfigurable topology is achieved by equipping each cell with two semiconductor switches. The switches are controlled by the battery management system (BMS) to either engage or bypass individual cells without interrupting the current path through the string. In the example shown in Figure 1, Cell 1 and Cell 27 are engaged, while Cell 2 is bypassed. The optimal cell configuration for each string is chosen according to two objectives. The first objective is to provide the required voltage and current levels for EV and inverter. This is specifically crucial for the EV charging process as no DC-DC converter is used to control the power flow according to the EV request. If the cell switching approach fails to meet the request with the necessary accuracy, the EV could open the contactor and terminate the charging procedure. The second objective is to balance the state-of-charge (SOC) of the different cells and keep them within a certain tolerance band. Hence, the BMS ensures safe performance of the whole battery while operating all cells according to their individual performance.
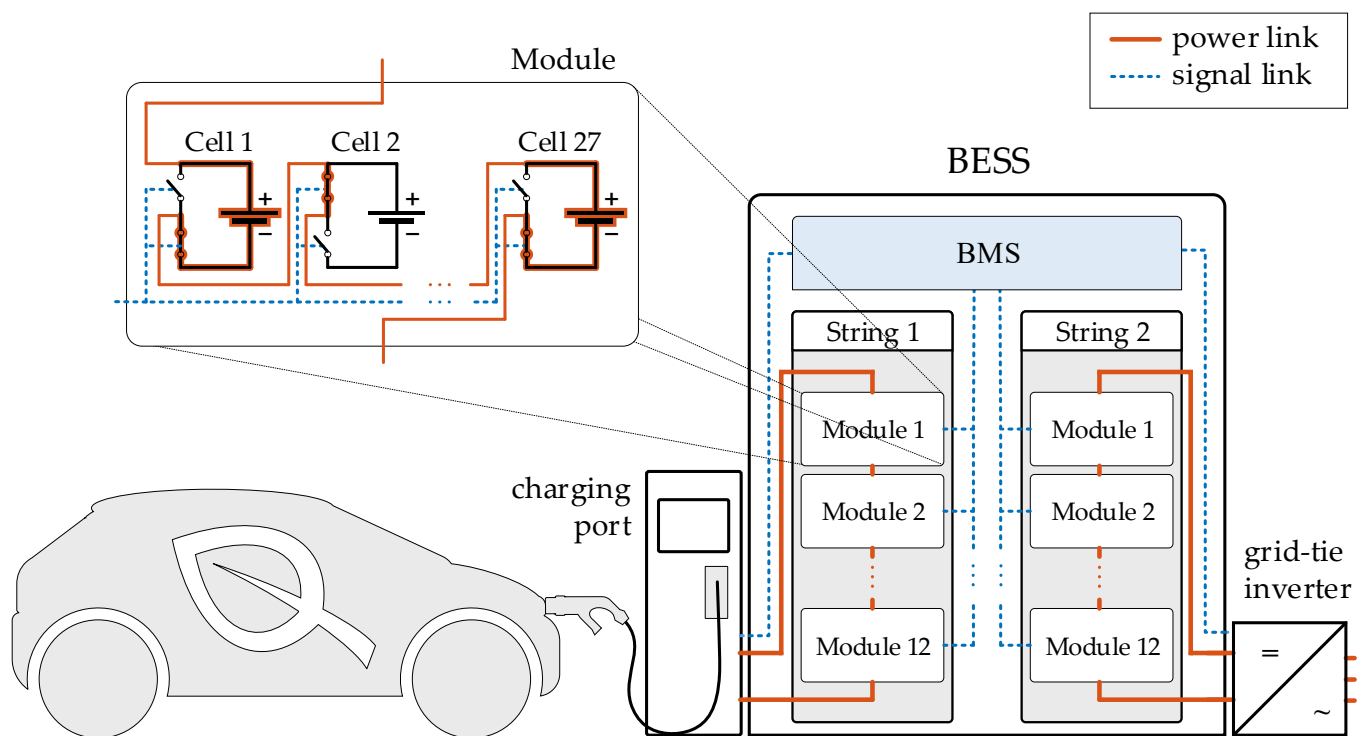

Figure 1. Schematic system overview of double-string BESS operated as an EV fast charging station.

The vehicle considered in the present study is the Nissan Leaf 2018 with CHAdeMO charging method. Therefore, the proposed design must fulfil the requirements for system configuration AA specified in charging standard IEC61851—Parts 23 and 24. Part 23 describes the technical specifications for DC electric charging stations [23], while Part 24 focuses on the digital communication between station and EV [24]. The standard was consulted to model the behaviour of the EV and to later assess whether the BESS could meet the charging request with sufficient accuracy.

It is noteworthy, as part of a joint activity between the EU-funded H2020 project INSULAE and the Danish funded EUDP project TOPchargE, the presented concept will be tested experimentally on the Danish island of Bornholm [25]. The BESS model described in Section 3 is therefore based on the properties of the real system in order to later validate the simulation results. Figure 2 shows the module prototype that will be deployed in the demonstration project. The used lithium-iron phosphate (LFP) cells have a nominal capacity of 100 Ah and a nominal voltage of 3.2 V [26]. With a total number of 324 cells, each of the strings has a nominal energy capacity of 104 kWh.

As seen in Figure 2, all cells are equipped with a controller that includes the semi-conductor switches used for engaging/bypassing as well as measurement devices for monitoring the cell state. Each switch consists of four metal–oxide–semiconductor field-effect transistors (MOSFETs) [27] that are operated in parallel in order to share the current. Additional information on the cell characteristics is given in the following section.
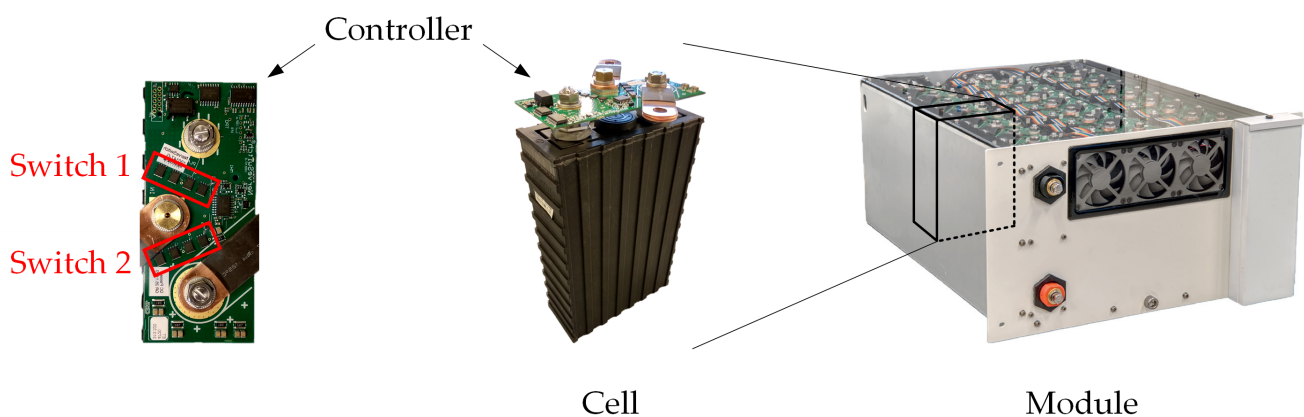
Figure 2. Prototype of a reconfigurable battery module. Each cell within the module is equipped with a controller that allows to either engage or bypass the cell.

3. Methodology

The proposed system was modelled in MATLAB & Simulink® [28], to assess the performance of the reconfigurable design. Figure 3 provides an overview of the modelling approach for double-string BESS, EV, and inverter. String 1 of the BESS is linked with the EV, while String 2 is linked with the grid-connected inverter. To provide clarification in the use of variables and parameters: time-dependent variables are written in italics, while parameters are written in roman (upright) font. The superscripts "BESS", "EV", and "Inv" are used to indicate to which unit a variable/parameter corresponds. Similarly, the subscripts "str1" and "str2" are used in case a variable/parameter solely refers to one of the two BESS strings. In the following subsections, the three models and their linkages are described in detail.
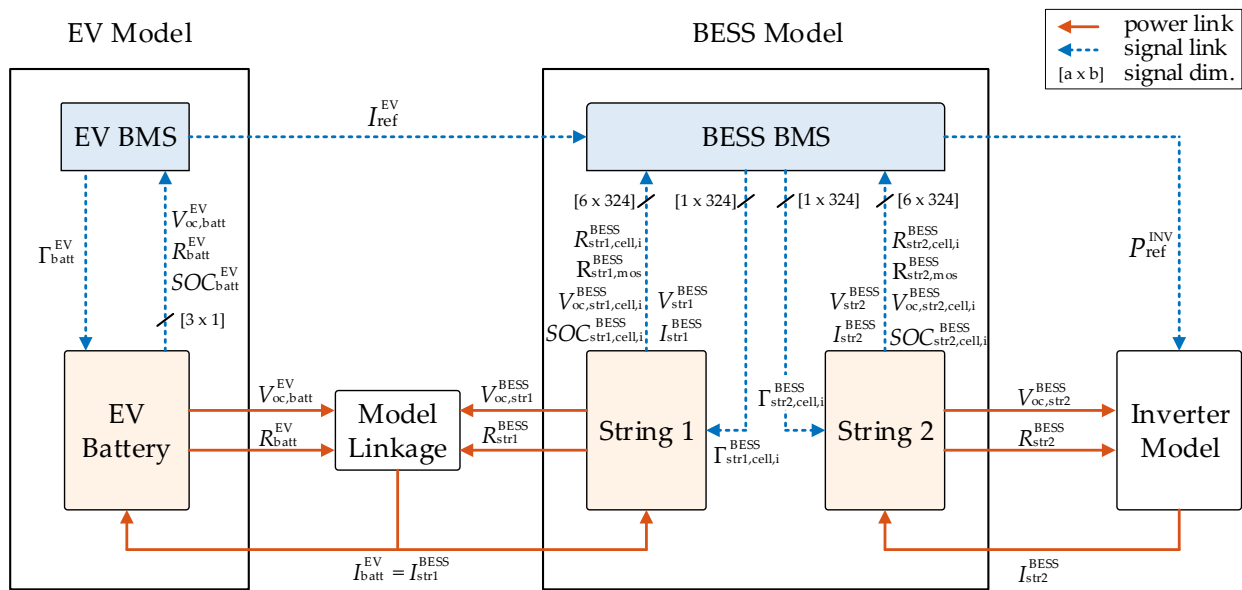
Figure 3. Overview of the models for BESS, EV, and inverter. Arrows show the data flow between the models: blue arrows indicate control/monitoring signals, orange arrows indicate information for calculating the power flow.

3.1. BESS Model

As illustrated in Figure 3, the BESS model comprises three submodels. The first submodel describes the behaviour of the BMS. The other two submodels are representing the physical properties of the two battery strings. As explained in Section 2, the two battery strings can be controlled independently by the BMS. Each string contains $N_{cell}^{BESS} = 324$ series-connected cells, which can be either engaged or bypassed depending on the control states of their individual switches. Table 1 summarises the specifications of the LFP cells. In order to capture the reconfigurable design of the battery string, each cell is modelled separately and can be identified by their cell number i. A binary control variable $\Gamma_{cell,i}^{BESS} \in \{0; 1\}$ is used to define whether a cell is engaged ("1") or bypassed ("0"). The electric cell behaviour is formulated as a Thévenin equivalent containing two elements: an open-circuit voltage $V_{oc,cell,i}^{BESS}$ and an internal cell resistance $R_{cell,i}^{BESS}$. The cell voltage is therefore given as

$$V_{cell,i}^{BESS} = V_{oc,cell,i}^{BESS} - I_{cell,i}^{BESS} \cdot R_{cell,i}^{BESS}, \tag{1}$$

where $I_{cell,i}^{BESS}$ is the cell current. The LFP cells were characterised in the laboratories of Nerve Smart Systems ApS in order to determine the SOC dependency of $V_{oc,cell,i}^{BESS}$ and $R_{cell,i}^{BESS}$. The estimation of the internal resistance was based on the voltage curve difference (VCD) method [29]. The obtained cell characteristics are presented in Figure 4. As seen in the graphs, the cells are only operated within SOC limits of 10% and 90% in order to prevent over- or undercharging.

The cell SOC changes when an electric current is applied. Since all cells in the battery string are connected in series, the cell current is a function of the total string current I_{str}^{BESS} and the individual connection state, given by $I_{cell,i}^{BESS} = I_{str}^{BESS} \cdot \Gamma_{cell,i}^{BESS}$. The sign convention of the current is defined so that positive values correspond to a discharging process. Hence, the cell SOC is calculated as

$$SOC_{cell,i}^{BESS} = -\frac{1}{C_{nom,cell,i}^{BESS}} \cdot \int I_{cell,i}^{BESS} dt + SOC_{init,cell,i}^{BESS}, \tag{2}$$

where $SOC_{init,cell,i}^{BESS}$ is the initial cell SOC at the beginning of the simulation. As shown in Figure 3 the individual cell states are monitored by the BMS, which is realised through a signal link from the respective *String* submodel to the *BESS BMS* submodel. Due to the series-connection, the electric behaviour of all cells within one string can be represented

by one single open-circuit voltage $V_{\text{oc,str}}^{\text{BESS}}$ and one resistance $R_{\text{str}}^{\text{BESS}}$. For the former, only engaged cells are contributing. Therefore, the string open-circuit voltage is given as

$$V_{\text{oc,str}}^{\text{BESS}} = \sum_{i=1}^{N_{\text{cell}}^{\text{BESS}}} \left(V_{\text{oc,cell,i}}^{\text{BESS}} \cdot \Gamma_{\text{cell,i}}^{\text{BESS}} \right). \tag{3}$$

The total string resistance comprises the resistances of the engaged cells and the on-state resistance of the switches. As previously mentioned, each switch consists of four MOSFETs that are operated in parallel. Given that the on-state resistance of each MOSFET is $0.58\,\text{m}\Omega$ [27], one switch is considered with a combined resistance of $R_{\text{mos}}^{\text{BESS}} = 0.145\,\text{m}\Omega$. Since one of the two switches per cell is always active in order to either engage or bypass the respective cell, the total string resistance is calculated as

$$R_{\text{str}}^{\text{BESS}} = \sum_{i=1}^{N_{\text{cell}}^{\text{BESS}}} \left(R_{\text{cell,i}}^{\text{BESS}} \cdot \Gamma_{\text{cell,i}}^{\text{BESS}} + R_{\text{mos}}^{\text{BESS}} \right). \tag{4}$$

The two variables $V_{\text{oc,str}}^{\text{BESS}}$ and $R_{\text{str}}^{\text{BESS}}$ are used for linking the BESS model to the respective models of the EV and the inverter, which are further described in Sections 3.2 and 3.3.
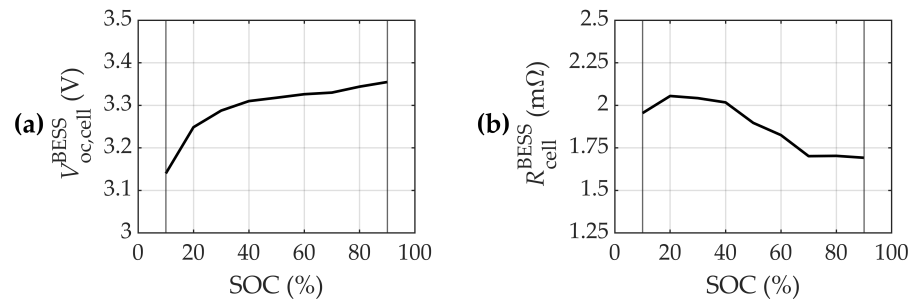

Figure 4. Cell characteristics of a 100 Ah LFP cell. The graphs show the obtained SOC dependency at $25\,^{\circ}\text{C}$ for: (**a**) open-circuit voltage; (**b**) cell resistance. The cells are operated within SOC limits of 10% and 90%.

Table 1. BESS cell specifications.

Nominal cell capacity	$C_{\text{nom,cell}}^{\text{BESS}}$	100 Ah
Nominal cell voltage	$V_{\text{nom,cell}}^{\text{BESS}}$	3.2 V
Maximum cell current	$I_{\text{max,cell}}^{\text{BESS}}$	200 A
MOSFET resistance	$R_{\text{mos}}^{\text{BESS}}$	$0.145\,\text{m}\Omega$
Cells per string	$N_{\text{cell}}^{\text{BESS}}$	324

Submodel *BESS BMS* contains the controlling algorithm, which is responsible for estimating the optimal connection state of each cell $\Gamma_{\text{cell,i}}^{\text{BESS}}$. Figure 5 provides a graphical overview of the algorithm. It is executed for each string separately and takes as an input the cell states as well as reference values for string voltage $V_{\text{ref,str}}^{\text{BESS}}$ and current $I_{\text{ref,str}}^{\text{BESS}}$. For String 1, the reference current $I_{\text{ref,str1}}^{\text{BESS}} = I_{\text{ref}}^{\text{EV}}$ is provided by the connected EV as defined in charging standard IEC61851-24 [24]. The corresponding reference voltage is estimated as $V_{\text{ref,str1}}^{\text{BESS}} = V_{\text{str1}}^{\text{BESS}} + \Delta V$, based on the measured string voltage $V_{\text{str1}}^{\text{BESS}}$ and an offset ΔV. This offset aims at correcting the current string voltage to reduce the difference between $I_{\text{ref,str1}}^{\text{BESS}}$ and $I_{\text{str1}}^{\text{BESS}}$. It is calculated as $\Delta V = (I_{\text{ref,str1}}^{\text{BESS}} - I_{\text{str1}}^{\text{BESS}}) \cdot R_{\text{str1}}^{\text{BESS}}$ and limited to values between $\Delta V \in [-1\,\text{V}; 1\,\text{V}]$ in order to avoid toggling effects in the cell control. For String 2, the voltage reference is set to the DC link voltage of the inverter while the reference current is set according to the desired power setpoint for the inverter $P_{\text{ref}}^{\text{Inv}} = V_{\text{ref,str2}}^{\text{BESS}} \cdot I_{\text{ref,str2}}^{\text{BESS}}$, as further discussed in Section 3.3.
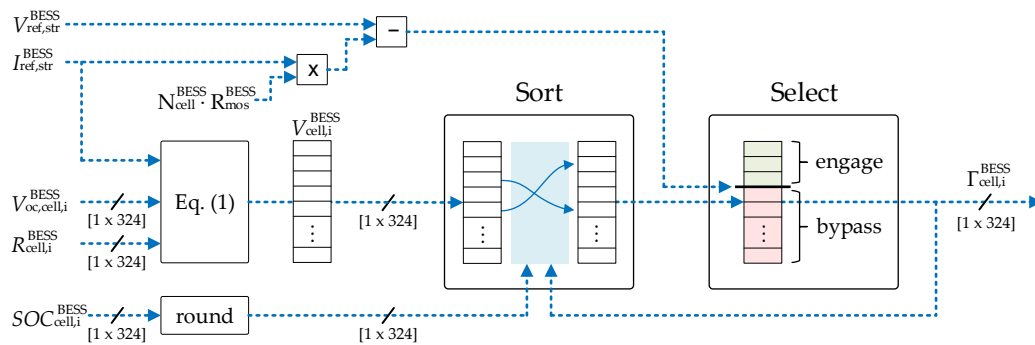
Figure 5. Graphical overview of the controlling algorithm. Based on cell states and reference values for string current and voltage, the algorithm estimates the optimal connection state for each individual cell.

Based on the monitored cell states $V_{oc,cell,i}^{BESS}$ and $R_{cell,i}^{BESS}$ of the corresponding string, the algorithm first creates a vector containing all predicted cell voltages in engaged state using (1) with $I_{cell,i}^{BESS} = I_{ref,str}^{BESS}$. As shown in Figure 5, the decision-making process is then divided into two steps: *Sort* and *Select*. In the first step, the vector with the predicted cell voltages is sorted according to their respective cell SOC. For discharging processes the sorting is done in decreasing order, thus voltages corresponding to cells with higher SOC will be sorted above the ones with lower SOC. For charging processes the sorting order is reversed. In the second step *Select*, the sorted vector is used to decide which cells to engage. Starting from the first element, the required number of cells is chosen in order to meet the reference voltage, taking into account the voltage drop along the semiconductor switches. The selected cells will get engaged, while the remaining ones will get bypassed. Consequently, the cells engaged during discharging processes are always the ones with the highest SOC. In contrast, cells with a low SOC will be prioritized during charging processes. By this the BMS ensures a balanced SOC level across the battery string. The overall number of switching processes is reduced by including a tolerance band defining the maximum allowed SOC difference between all cells of the same string. As seen in Figure 5, this is realized by rounding the SOC values in defined steps (e.g., 5%) before applying them in the sorting algorithm. For cells with the same rounded SOC value, the ones that are currently engaged are prioritized. Consequently, cells remain in their current connection state until they leave the defined SOC band. The process of executing the algorithm including the cell switching action is considered with a total delay of 0.1 s.

3.2. EV Model

As seen in Figure 3, the EV model consists of two submodels. *EV BMS* is responsible for monitoring the EV battery state and sending the charging request to the charging station. *EV battery* describes the physical state of the EV battery and is based on the features of the Nissan Leaf 2018, which was characterised by Calearo et al. [30]. The specifications of the EV battery are given in Table 2. Similar to the BESS, the electrical behaviour is formulated as a Thévenin equivalent comprising an open-circuit voltage $V_{oc,batt}^{EV}$ and a resistance R_{batt}^{EV}. Figure 6 shows the SOC dependencies of both variables.

Table 2. EV battery specifications.

Nominal battery capacity	$C_{nom,batt}^{EV}$	112.6 Ah
Nominal battery voltage	$V_{nom,batt}^{EV}$	350.4 V
Minimum battery voltage	$V_{min,batt}^{EV}$	290 V
Maximum battery voltage	$V_{max,batt}^{EV}$	405 V
Maximum ref. current (1C)	$I_{ref,max}^{EV}$	112.6 A
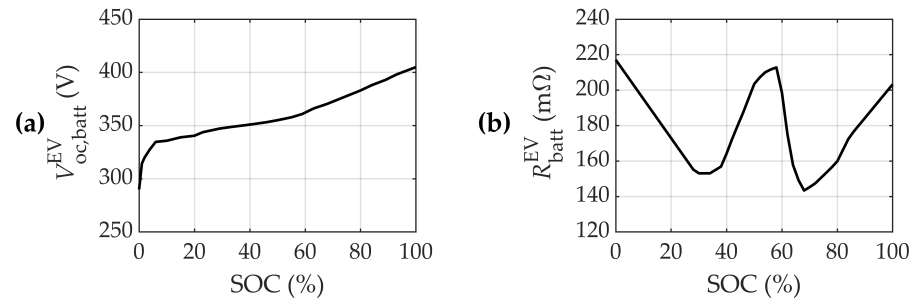
Figure 6. Characteristics of the EV battery. The graphs show the obtained SOC dependency at 30 °C for: (**a**) open-circuit voltage; (**b**) battery resistance.

During the charging process, the EV SOC is subject to the electric current provided by String 1, with $I_{batt}^{EV} = I_{str1}^{BESS}$. The sign convention is defined so that positive values lead to an increase of the SOC according to

$$SOC_{batt}^{EV} = \frac{1}{C_{batt}^{EV}} \int I_{batt}^{EV} dt + SOC_{init,batt}^{EV}, \tag{5}$$

where $SOC_{init,batt}^{EV}$ is the initial SOC at the beginning of the simulation. The battery states are monitored by the EV BMS which is realized through a signal link between the two submodels. In return, the EV BMS can control the state of the EV contactor that links the EV battery to the charging station using the binary control variable $\Gamma_{batt}^{EV} \in \{0;1\}$. The contactor is closed ("0" to "1") after authentication and information exchange between EV and charging station were successfully completed [24]. During the power transfer, submodel *EV BMS* calculates the optimal setpoint for the charging current based on the battery state and communicates this reference value to the charging station. In principle, the fast charging process can be divided into two stages: constant current charging and constant voltage charging. In the former, the reference current is kept at its maximum $I_{ref}^{EV} = I_{ref,max}^{EV}$. To maintain this value, the charging station will continuously increase the voltage at the terminals, as the EV open-circuit voltage increases with rising charge level. Once the charging voltage reaches the maximum battery voltage $V_{batt,max}^{EV}$, the requested charging current decreases according to

$$I_{ref}^{EV} = (V_{batt,max}^{EV} - V_{oc,batt}^{EV}) / R_{batt}^{EV}. \tag{6}$$

This phase is referred to as the constant voltage stage, since the charging voltage is kept at the maximum $V_{batt,max}^{EV}$. The actual charging current is calculated in the *Model Linkage* as seen in Figure 3. The block takes as an input the values of the Thévenin equivalents of both the EV and the BESS string model. Based on these inputs, the current is calculated as

$$I_{batt}^{EV} = I_{str1}^{BESS} = \frac{V_{oc,str1}^{BESS} - V_{oc,batt}^{EV}}{R_{str1}^{BESS} + R_{batt}^{EV}}. \tag{7}$$

The charging current is later compared to the reference current in order to assess whether the control concept of the BESS complies with the accuracy defined in standard IEC61851-23.

3.3. Inverter Model

The inverter is used for recharging the BESS. In the present setup it is connected to String 2. The BESS controls the DC link voltage between the two units according to a fixed reference value of $V_{ref,str2}^{BESS} = 650$ V. The inverter is responsible for controlling the power flow from the grid according to the setpoint P_{ref}^{Inv} provided by submodel *BESS BMS*. It is considered as an ideal power source that, depending on the actual DC link voltage,

supplies the required current to meet the reference power. The resulting string current is calculated as

$$I_{\text{str2}}^{\text{BESS}} = \frac{V_{\text{oc,str2}}^{\text{BESS}}}{2 \cdot R_{\text{str2}}^{\text{BESS}}} - \sqrt{\left(\frac{V_{\text{oc,str2}}^{\text{BESS}}}{2 \cdot R_{\text{str2}}^{\text{BESS}}} \right)^2 - \frac{P_{\text{ref}}^{\text{Inv}}}{R_{\text{str2}}^{\text{BESS}}}}. \tag{8}$$

It should be noted that the sign convention for the reference power is the same as for the BESS string current: negative power values correspond to charging, thus leading to an increase of the string SOC.

4. Case Study

The case study is designed to investigate three different aspects of the reconfigurable design. First, the performance of the BESS when controlling the EV charging process will be assessed. Second, the capability of balancing the SOC of all cells within the same string is validated for both charging and discharging. Third, the efficiency of the system will be estimated. In the following, the model settings for BESS, EV, and inverter are defined.

4.1. BESS Settings

String 1 is connected to the EV, while String 2 is connected to the inverter. In the BMS, the allowed SOC band is set to 5% for each of the two strings. Hence, the controlling algorithm must ensure that the SOC difference between the highest- and the lowest-charged cell does not exceed this value. String 1 is considered to be at the upper charge limit. The initial SOC of the individual cells in String 1 is generated randomly with a uniform probability distribution within the limits of 85% and 90%. Hence, at the beginning of the simulation, the SOC of all cells are within the defined 5 % band. In contrast, the initial SOC of the cells in String 2 will take random values within limits of 10% and 30%, thus exceeding the tolerance band. This allows for the verification of whether the BMS is able to bring the cell SOC differences in String 2 back into the defined SOC band during the recharging process.

4.2. EV Settings

The EV battery is completely discharged at the beginning of the simulation with $\text{SOC}_{\text{init,batt}}^{\text{EV}} = 0\%$. The vehicle has an available charging time of 70 min and expects to reach a target SOC of 95 % after this time window. It is assumed that authentication and initial communication between charging station and EV were completed successfully before the start of the simulation. At $t = 0\,\text{s}$, the vehicle will close the contactor ($\Gamma_{\text{batt}}^{\text{EV}} = 1$) and start to send a request for the charging current, which will be updated every 100 ms [24]. At the beginning of the charging procedure, the EV will request the charging station to ramp up the charging current with the maximum allowed rate of change of 20 A/s [23]. The rest of the charging procedure will be carried out in stages of constant current and constant voltage charging, as previously described in Section 3.2.

4.3. Inverter Settings

The power setpoint $P_{\text{ref}}^{\text{Inv}}$ of the inverter is held at a constant value of 22 kW throughout the simulation. This value corresponds to the rated power of a grid connection in a 3-phase distribution grid with a nominal voltage of 230 V and a rated current of 32 A per phase. Since the focus of the study is on the battery system, power losses in the inverter are not considered.
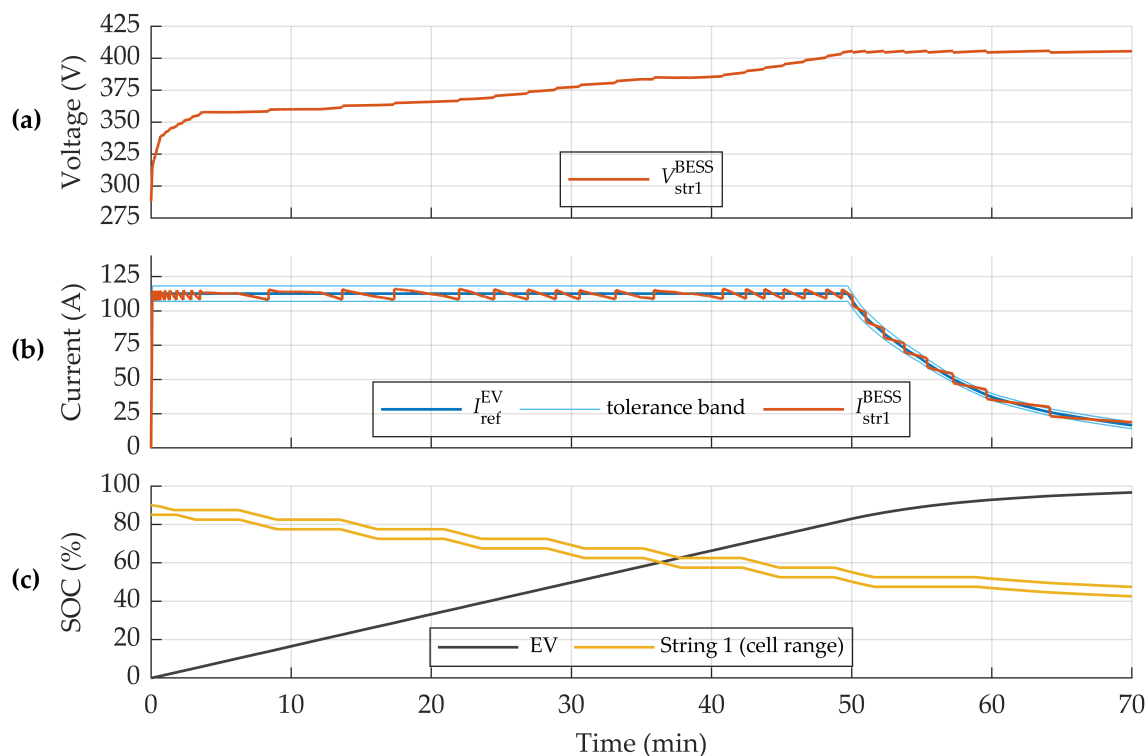
5. Results

In this section, the simulation results are presented. The simulation was performed with a fixed time-step of 10 ms. The following analysis is divided into three parts. The first part is evaluating the EV charging process. Particular focus is given to the accuracy of the current control, with respect to the charging request sent by the vehicle. In the second part,

the capability of the reconfigurable design to balance the charge level is assessed. In the third part, the efficiency of the proposed system is determined.

5.1. EV Charging

Figure 7 provides an overview of the progressions of voltage, current, and SOC during the EV charging procedure. As defined in the case study, the EV has an initial SOC of 0% while the cells of String 1 have an initial SOC between 85% and 90%. In this regard, the two lines for String 1 in Figure 7c are indicating the range between the highest and lowest cell SOC. At $t = 0\,\text{s}$ the energy transfer to the EV starts. The charging procedure can be divided into two stages. During the constant current stage, the charging current was kept at its maximum while the voltage was increasing from its initial value of 290 V to the maximum EV battery voltage of 405 V. During this stage, the vehicle SOC was increasing linearly from 0% to 83% within 50 min. At this point in time, the voltage applied by String 1 reached the maximum EV battery voltage which initiated the constant voltage stage. Here, the voltage was held at its maximum while the charging current $I_{\text{str1}}^{\text{BESS}}$ declined. As a result, the EV SOC was increasing more slowly. After the charging time of 70 min the EV reached a final SOC of 97%, thus fulfilling the charging goal. The overall charge level of String 1 decreased to an average value of 47%. Throughout the charging procedure, the BESS was able to keep the cells within the allowed SOC range of 5%, as seen by the progressions of maximum and minimum cell SOC. This aspect is further discussed in Section 5.2.

Figure 7. Simulation results of the EV fast charging process: (**a**) charging voltage; (**b**) comparison of actual charging current and reference current requested by EV; (**c**) SOC of EV and String 1. For String 1, the progressions of the highest and the lowest cell SOC are shown.

Figure 7b compares the charging current $I_{\text{str1}}^{\text{BESS}}$ to the reference value requested by the EV. As seen in the plot, the BESS was able to follow the request during both charging stages. This demonstrates the general capability of controlling the charging current by adapting the number of engaged cells, without the need of any power converter. However, in order to operate as a public fast charging station, the charging current must be controlled with sufficient accuracy. According to charging standard IEC61851-23, the current request sent by the EV must be fulfilled within limits of $\pm 2.5\,\text{A}$ for $I_{\text{ref}}^{\text{EV}} < 50\,\text{A}$, and $\pm 5\,\%$ for

$I_{\text{ref}}^{\text{EV}} > 50\,\text{A}$ [23]. A permitted time delay for initiating the control action is specified as 1 s after receiving a new reference value. The resulting tolerance band is indicated in Figure 7b in order to compare the simulation results to the standard. Additionally, Figure 8 provides a closer view of the current ramp-up at the beginning of the charging procedure. As defined in the case study, the EV requested an increase of the current with 20 A/s and updated the value every 100 ms. The maximum current request of $I_{\text{ref,max}}^{\text{EV}} = 112.6\,\text{A}$ was therefore received after 5.7 s. As seen in the plot, the charging current provided by String 1 followed the reference value and stayed within the tolerance band. In addition, during the constant current stage shown in Figure 7b the charging request was met with sufficient accuracy. However, deviations between reference and actual current are visible. During this stage, the current followed the progression of a reverse sawtooth function characterised by a step-wise increase followed by a linear decrease. After entering the constant voltage stage, the current was decreasing in a step-wise fashion with intermediate sections of linear decline. Towards the end of the charging procedure, the tolerance band was occasionally exceeded.
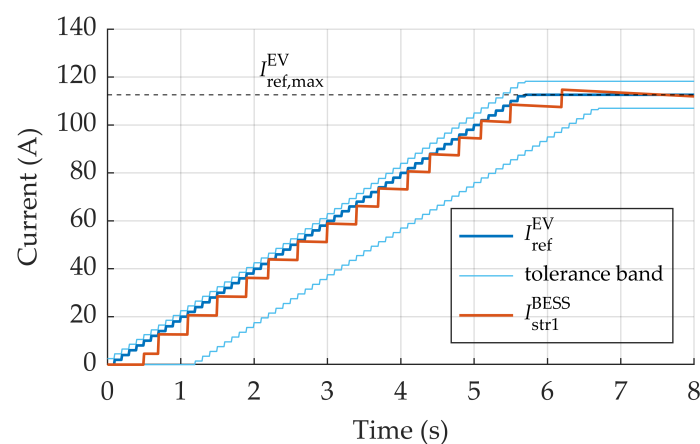
Figure 8. Comparison of actual charging current $I_{\text{str1}}^{\text{BESS}}$ and reference current $I_{\text{ref}}^{\text{EV}}$ at the beginning of the fast charging process. The tolerance band is indicating the maximum allowed deviation from the requested value.

To further improve the technology it is therefore necessary to analyse the origin of the current deviations. Figure 9 provides a closer view of the progressions of voltage and current for an exemplary time window at the end of the constant current stage. Besides the progression of the charging voltage $V_{\text{str1}}^{\text{BESS}}$ at the connection point between BESS and EV, the plot shows the open-circuit voltages of both String 1 and EV. The difference between $V_{\text{oc,str1}}^{\text{BESS}}$ and $V_{\text{str1}}^{\text{BESS}}$ is equivalent to the voltage drop at the total string resistance $R_{\text{str1}}^{\text{BESS}}$, and the difference between $V_{\text{str1}}^{\text{BESS}}$ and $V_{\text{oc,batt}}^{\text{EV}}$ is equivalent to the voltage drop at the resistance $R_{\text{batt}}^{\text{EV}}$ of the EV battery. As seen in the graph, the vehicle voltage $V_{\text{oc,batt}}^{\text{EV}}$ shows a continuous progression, while $V_{\text{str1,oc}}^{\text{BESS}}$ is increasing incrementally. These steps are a result of the cell switching performed by the BESS. In order to maintain a steady level of the charging current, the controlling algorithm successively engages more cells to provide the necessary voltage difference to the EV. During the shown time interval, six additional cells were engaged, apparent from the corresponding number of voltage steps. Similarly, the engagement of an additional cell leads to a stepwise increase of the charging current as seen in Figure 9b. This can be explained by looking at Equation (7). Since the charging current is a function of the voltage difference between $V_{\text{oc,str1}}^{\text{BESS}}$ and $V_{\text{oc,batt}}^{\text{EV}}$ divided by the total resistance in the circuit, the increment of $V_{\text{oc,str1}}^{\text{BESS}}$ is directly reflected in the current progression. After each step, the continuous increase of $V_{\text{oc,batt}}^{\text{EV}}$ leads to a decrease of the charging current as the voltage difference $V_{\text{oc,str1}}^{\text{BESS}} - V_{\text{oc,batt}}^{\text{EV}}$ becomes smaller until it is required to add another cell. As a result, the current will follow the inverse sawtooth progression already observed in Figure 7b.

This analysis underlines the importance of a precise control of the string voltage, as steps in the string voltage are directly reflected in the current progression. Furthermore, the magnitude of the current deviations is influenced by the vehicle resistance. Since this resistance is dependent on various aspects, such as the car model, battery SOC, and temperature, the investigated control approach may not fulfil the required accuracy under all circumstances. Based on those findings, further improvements of the technology aiming at decreasing the current deviations will be suggested in Section 6.
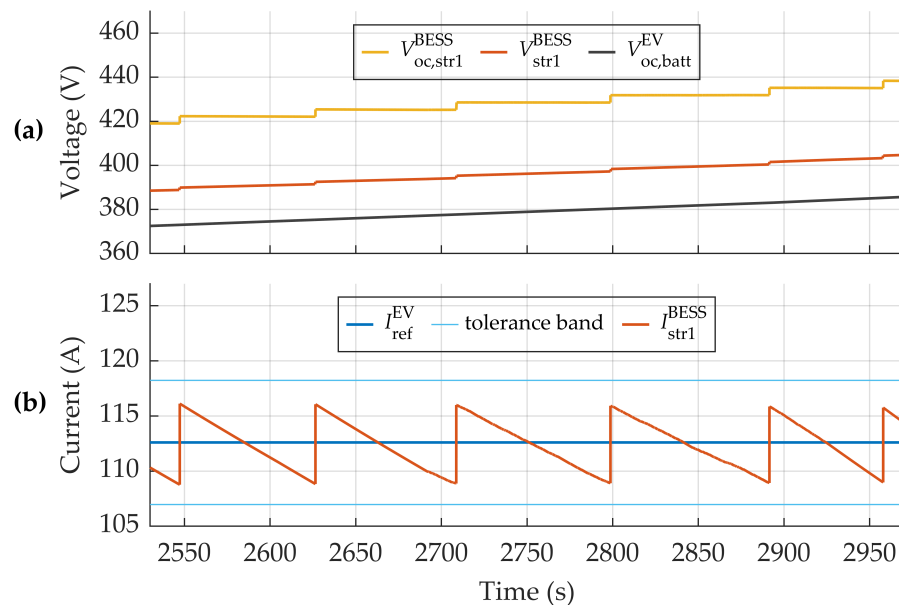

Figure 9. Progressions of voltage and current at the end of the constant current stage: (**a**) voltages at different points in the system; (**b**) comparison of charging current $I_{\text{str1}}^{\text{BESS}}$ and reference value $I_{\text{ref}}^{\text{EV}}$. The tolerance band is indicating the maximum allowed deviation from the vehicle request.

5.2. SOC Balancing

During operation, the BESS adapts the number of engaged cells in order to provide the required voltage levels for EV and inverter. Engaged cells will therefore experience a change in their SOC, while the SOC of bypassed cells remains constant. The controlling algorithm ensures that the SOC difference between cells of the same string will stay within a defined tolerance band. In the case study, this band was defined as 5 % for both charging and discharging. Figure 10 demonstrates the principle according to which the BMS balanced the string SOC in the performed simulation. Plots (a1) and (b1) relate to String 1 and show the progressions of power and SOC, respectively. Similarly, plots (a2) and (b2) show the progressions of power and SOC of String 2.

For String 1, the power is given as the product $V_{\text{str1}}^{\text{BESS}} \cdot I_{\text{str1}}^{\text{BESS}}$. Consequently, the current deviations discussed in Section 5.1 are also reflected in the power progression. During constant current charging, the power keeps increasing due to the rise in the voltage. The maximum power value of 46.8 kW is reached at the end of this charging phase where both voltage and current are maximum. At this point in time, a total number of 132 cells is engaged. During constant voltage charging, the power declines due to the decreasing charging current. In plot (b1) and (b2), each line represents the SOC progression of one single cell which allows to demonstrate the cell balancing method. The line colour indicates in which module the cell is located. As defined in the case study, the cells in String 1 have a random initial SOC between 85 % and 90 %. The connection state of the cells can be identified through their individual SOC trend. Due to the discharging process, the SOC of an engaged cell is declining while the SOC of a bypassed cell remains constant. To maintain a balanced charge level across the string, the controlling algorithm makes sure that newly engaged cells are always the ones with the highest SOC. These cells remain

engaged until their SOC reaches the lower limit of the defined SOC band. At this point, they will get bypassed and replaced by cells from the upper limit of the SOC band. Bypassed cells remain disconnected until they become the cells with the highest SOC due to the discharging of other cells. Hence, the controlling algorithm utilizes the flexibility within the SOC band to minimize the number of switching events per cell. The behaviour described above leads to the distinctive SOC profile seen in subplot (a2). The progression of the band can be described as a step-wise decrease, where sections with linear decline are followed by plateaus with constant SOC levels. The plateaus occur every 5 %, which corresponds to the width of the SOC band. During the constant voltage stage, the SOC is decreasing slower due to the declining charging power. At the end of the simulation, String 1 reached an average charge level of 47 %.
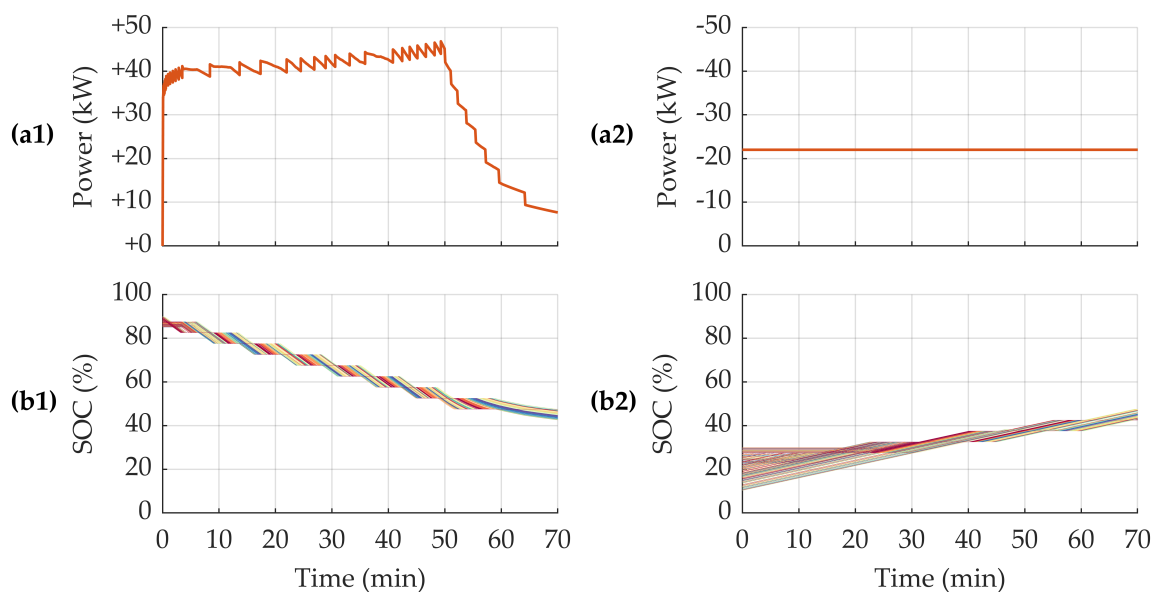
Figure 10. Simulated progressions of power and SOC for both strings: (**a1,b1**) show the power and SOC progression for String 1, respectively; (**a2,b2**) show the power and SOC progression for String 2, respectively. In the SOC graphs, each line represents the SOC progression of one single cell. Line colours indicate cells of the same module.

While String 1 is discharging, String 2 is getting recharged with a constant power of 22 kW by the grid-connected inverter. As described in the case study, the initial SOC values of String 2 were generated randomly with a uniform probability distribution between 10% and 30%. This allows to assess whether the reconfigurable BESS is able to bring the SOC differences back into the defined 5% band. As seen in subplot (b2), the controlling algorithm is pursuing this by prioritising cells with lower SOC values when deciding which cells to engage. Consequently, the SOC of low-charged cells is increasing while cells with a high SOC stay at their initial value. Hence, the controlling algorithm is "lacing" together the cell SOC across String 2 and bringing them back into the defined 5% band. From this point, the overall string SOC progression follows the same characteristic seen for String 1 but with increasing trend. The rate of change of the charge level is lower than for String 1, since the absolute value of the charging power is set lower than the discharging power. After a simulation time of 70 min, String 2 reached an average charge level of 44%. Throughout the charging process, an average number of 193 cells were engaged.

All in all, the results show that the reconfigurable BESS can maintain a balanced SOC of the individual cells during both charging and discharging processes. Furthermore, the controlling algorithm is able to regain a balanced charge level of strings with initially unbalanced cell states.

5.3. System Efficiency

Figure 11 provides an overview of the energy that got transferred between the different components. During the EV charging process, a total energy amount of 41.09 kWh was transferred from String 1 to the vehicle. Of this energy, 39.08 kWh could be stored in the EV battery, while 2.01 kWh were dissipated as heat. Thus, the estimated EV efficiency is 95.1 %. To provide the required energy, 44.06 kWh were extracted from the cells in String 1. Consequently, the BESS efficiency during the EV charging process was 93.3 %. The losses can be divided into losses generated by cells and MOSFETs which amount to 2438 Wh and 536 Wh, respectively. Hence, the energy loss caused by the MOSFETs corresponds to 1.2 % of the total energy extracted from String 1.

While String 1 was providing charging power to the EV, String 2 was getting recharged. The total energy amount provided by the grid-connected inverter was 25.67 kWh. From this value, 25.08 kWh could be stored in String 2. Consequently, the efficiency for recharging String 2 was 97.7 %. The losses caused by cell resistances and MOSFETs were 524 Wh and 63 Wh, respectively. Hence, the energy losses caused by the MOSFETs corresponds to 0.25 % of the total energy provided by the grid-connected inverter. The higher efficiency of String 2 compared to String 1 can be explained by the lower current. With a fixed power setpoint of $P_{\text{ref}}^{\text{Inv}} = -22$ kW and a DC link voltage of $V_{\text{str2}}^{\text{BESS}} = 650$ V, the mean absolute value of the current in String 2 was 33.8 A. As the Joule losses in cells and MOSFETs are proportional to the square of the current, the total losses in String 2 were significantly lower than in String 1. Considering the achieved efficiencies for String 1 and String 2, the overall round trip efficiency of the BESS was 91.1 %.
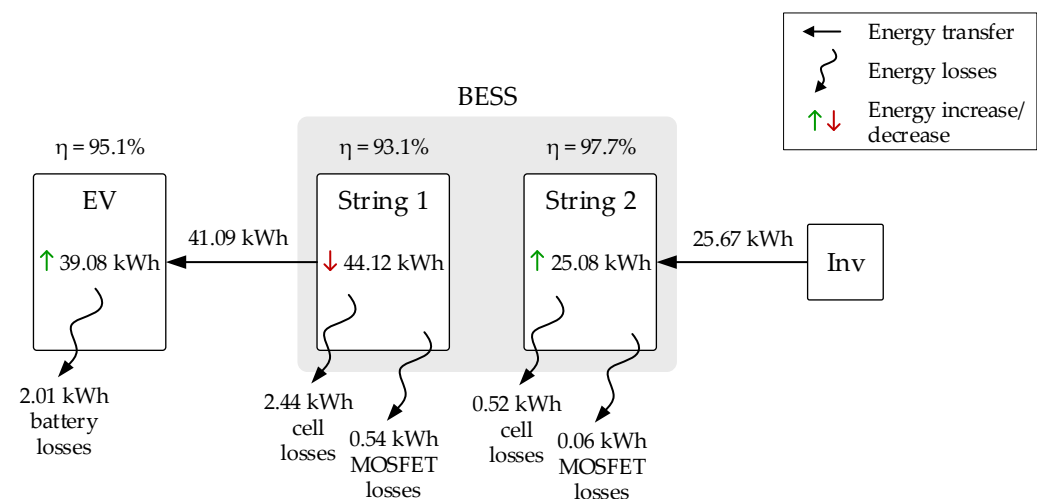
Figure 11. Overview of transferred energy and power losses in the system.

It should be noted that the presented model only considered the on-state resistance of the MOSFETs for calculating the losses caused by the reconfigurable design. Resistances of cell controllers and wiring were not characterised and could therefore not be included. Furthermore, switching losses of the MOSFETs were neglected. The latter are not expected to add a significant contribution, as the MOSFETs were not switched at high frequency. In fact, the cells in String 1 and String 2 changed their connection state in average 11 and 8 times, respectively. However, future investigations with a stronger focus on the system efficiency should consider these aspects.

6. Discussion

The results suggest that a reconfigurable battery is generally able to control the power transfer to an EV without the need of a DC-DC converter interconnected between the two units. By adapting the number of engaged cells in a real-time fashion, the BESS could fulfil the EV request with sufficient accuracy for most of the charging process. However, the analysis revealed that engaging and bypassing individual cells only allows for coarse

control of the battery string voltage. This can lead to significant variations of the charging current. To avoid this, a more precise control of the string voltage has to be achieved. One conceptual measure with respect to the BESS design could be to use cell types with a lower open-circuit voltage, such as lithium titanate oxide (LTO) or absorbed glass mat (AGM) cells. Another approach focused on the controlling algorithm could be to allow a larger range of the cell SOC. This would result in more diverse cell voltages that are then utilized to control the overall string voltage with a higher accuracy. Besides that, an additional hardware element for precise voltage control could be connected in series to the battery string. This task could be taken by a differential power processing converter with an output voltage range of 5 V, which is enough to complement the coarse voltage control achieved by the cells. A similar approach is applied in photovoltaic (PV) systems to balance the voltage output of PV elements with mismatched production [31].

For the system analysed in the present study, 1.2% of the energy provided by String 1 is lost through the MOSFETs that are used to achieve the reconfigurable design. Since the proposed battery design does not require a DC-DC converter for controlling the EV charging process, the additional losses caused by the MOSFETs can be compared against the saved converter losses. The achieved efficiency of DC-DC converters used in fast charging stations lies around 96–98% [32,33]. Hence, the proposed system has a competitive efficiency compared to a battery buffered fast charging station with power converter. In addition, the reconfigurable design allows for the adaptation the string voltage to any EV voltage level and is therefore suitable for charging processes at both 400 V and 800 V. Regardless of the required voltage, the number of active switches stays the same as always one switch per cell is active for either engaging or bypassing the respective cell. Consequently, the losses of the MOSFETs are generally independent of the string voltage but depend only on the current. In contrast, the highest efficiency of DC-DC converters is achieved for a specific range of the output voltage [32].

The overall efficiencies for String 1 (EV charging) and String 2 (recharging) were determined as 93.3% and 97.7%, respectively. As clarified in Section 5.3, the lower efficiency of String 1 are a result of the overall higher current. One solution to reduce the Joule losses could be to operate String 1 as a parallel connection of two substrings with 6 modules each, in case the required voltage levels are below 500 V. By splitting the series connection of 12 modules into two parallel branches of 6 modules, all cells and current experience only half the current which reduces the power losses for EV charging significantly. Additionally, the losses during recharging can be reduced by increasing the DC link voltage of the inverter. For a fixed power setpoint this would result in a lower charging current and, consequently, lead to reduced power losses in both cells and MOSFETs.

The present case study demonstrates how the proposed BESS design decouples the dynamics of the fast charging process from the grid. The storage enables power levels above grid capacity, which reduces vehicle charging times significantly. However, it should be noted that enhanced power levels are only available if the BESS charge level is sufficiently high. In case of consecutive charging of several EVs, the decreasing BESS SOC would require the reduction of the EV charging power to the available grid capacity. Hence, it is important to size the BESS according to both the expected EV usage and the grid capacity at the respective location.

For future analyses, the existing model could be further developed. To gain a more comprehensive understanding of the dynamics that occur during cell switching events, the cell behaviour can be formulated as a second-order Thévenin model. This approach considers RC branches in the model to represent the transient response of the cells [34,35]. Additionally, the electric characteristics of cell controllers and connecting elements (e.g., cables) should be included. With regard to the presented control algorithm, a more sophisticated version could also include temperature and state-of-health of the individual cells. Thus, preventive measures against overheating and diverging ageing processes of individual cells are considered in the decision-making process. The extended model can serve as the basis for a future study that compares a reconfigurable battery system to a conventional

battery system with DC-DC converter. This comparison could include a comprehensive assessment of investment costs and power efficiency for both systems.

Besides simulation studies, a prototype of the reconfigurable battery will be installed on the Danish island of Bornholm, which enables experimental validation of the presented simulation results. Furthermore, the demonstration project may reveal disadvantages of the reconfigurable design. Potential risks include short circuiting of cells due to MOSFET failure and transient currents when switching complete battery strings. Another concern is that cell switching during operation may have a negative impact on the lifetime of the battery. All in all, the prototype will allow us to investigate various aspects of the reconfigurable battery design, such as the overall system efficiency, control accuracy for EV charging processes, and battery degradation.

7. Conclusions

The present work introduces a novel design of a double-string BESS with reconfigurable cell topology, that is operated as an EV fast charging station. One string is providing charging power to an EV, while the other string is recharged through a grid-connected inverter. This approach enables power levels above grid capacity, which reduces vehicle charging times significantly. Each battery cell is equipped with MOSFETs that allow for either the engagement or bypass of the respective cell. The reconfigurability is used to directly control the power transfer to the EV by adapting the number of engaged cells in a real-time fashion. Hence, the proposed design does not require any DC-DC converter as interface to the EV. The paper describes in detail a modelling approach of the reconfigurable battery, including the controlling algorithm used for cell engagement. The simulation results show that the BESS is able to fulfil the EV request with sufficient accuracy for most of the fast charging process. However, the switching of cells causes voltage steps that can potentially lead to variations in the charging current. During the end of the simulated charging process, these current deviations occasionally exceeded the tolerance band defined in charging standard IEC61851-23. Therefore, complementary measures are suggested to achieve a suitable current control during all phases of the charging process.

The reconfigurable topology is further utilised to balance the SOC of the individual cells. The proposed control is able to keep all cells of the same string within a defined 5% SOC band during both charging and discharging. The simulation results showed a BESS efficiency of 93.3% during the EV fast charging process. The losses caused by the MOSFETs amount to 1.2% of the provided energy. Hence, the concept of controlling the EV charging process through adapting the cell configuration is competitive compared with the efficiency of a DC-DC converter. The BESS efficiency during recharging was 97.7%, resulting in a round trip efficiency of 91.1%. As a next step, the simulation results will be validated experimentally in a demonstration project on the Danish island of Bornholm.

Author Contributions: Conceptualisation, J.E., J.M.Z., T.G., G.R. and M.M.; methodology, J.E., J.M.Z., T.G., G.R. and M.M.; software, J.E.; formal analysis, J.E.; investigation, J.E.; writing—original draft preparation, J.E.; writing—review and editing, J.E., J.M.Z., T.G., G.R. and M.M.; visualisation, J.E.; supervision, T.G. and M.M.; funding acquisition, M.M. All authors have read and agreed to the published version of the manuscript.

Conflicts of Interest: The authors declare no conflict of interest.

Abbreviations

The following abbreviations and symbols are used in this manuscript:

Abbreviations

AGM	Absorbed glass mat
BESS	Battery energy storage system
BMS	Battery management system
EV	Electric vehicle
LFP	Lithium iron phosphate
LTO	Lithium titanate oxide
MOSFET	Metal–oxide–semiconductor field-effect transistor
PV	Photovoltaics
SOC	State-of-charge

Symbols

C	Capacity (Ah)
I	Current (A)
N	Number of cells (-)
P	Power (W)
R	Resistance (Ω)
SOC	State-of-charge (%)
t	Time (s)
V	Voltage (V)
Γ	Connection state (1/0)
Δ	Difference (-)
η	Efficiency (%)

Symbol Indices

batt	EV battery
cell	BESS cell
i	Cell number
init	Initial value
max	Maximum value
min	Minimum value
mos	MOSFET
nom	Nominal value
oc	Open-circuit
ref	Reference value
str	BESS string

References

1. Kasten, P.; Bracker, J.; Haller, M.; Purwanto, J. *Assessing the Status of Electrification of the Road Transport Passenger Vehicles and Potential Future Implications for the Environment and European Energy System*; Specific Contract under Framework Contract EEA/ACC/13/003, Lot-1. Final report—Task 2; OEKO-Institut, Transport & Mobility Leuven, TNO, Trinomics: Berlin, Germany, 2016.
2. Brand, C.; Cluzel, C.; Anable, J. Modeling the uptake of plug-in vehicles in a heterogeneous car market using a consumer segmentation approach. *Transp. Res. Part A Policy Pract.* **2017**, *97*, 121–136. [CrossRef]
3. Zhang, Q.; Li, H.; Zhu, L.; Campana, P.E.; Lu, H.; Wallin, F.; Sun, Q. Factors influencing the economics of public charging infrastructures for EV—A review. *Renew. Sustain. Energy Rev.* **2018**, *94*, 500–509. [CrossRef]
4. Wolbertus, R.; den Hoed, R.V. Electric Vehicle Fast Charging Needs in Cities and along Corridors. *World Electr. Veh. J.* **2019**, *10*, 45. [CrossRef]
5. Simpson, M.; Markel, T. Plug-in electric vehicle fast charge station operational analysis with integrated renewables. In Proceedings of the International Battery, Hybrid and Fuel Cell Electric Vehicle Symposium 26 (EVS26), Los Angeles, CA, USA, 6–9 May 2012; pp. 1–8.
6. Mauri, G.; Valsecchi, A. Fast charging stations for electric vehicle: The impact on the mv distribution grids of the milan metropolitan area. In Proceedings of the 2012 IEEE International Energy Conference and Exhibition (ENERGYCON), Florence, Italy, 9–12 September 2012; pp. 1055–1059. [CrossRef]

7. Dharmakeerthi, C.H.; Nadarajah, M.; Mithulananthan, T. Impact of electric vehicle fast charging on power system voltage stability. *Int. J. Electr. Power Energy Syst.* 2014, 57, 241–249. [CrossRef]
8. Bryden, T.S.; Hilton, G.; Dimitrov, B.; de León, C.P.; Cruden, A. Rating a Stationary Energy Storage System Within a Fast Electric Vehicle Charging Station Considering User Waiting Times. *IEEE Trans. Transp. Electrif.* **2019**, *5*, 879–889. [CrossRef]
9. Simone, D.D.; Piegari, L. Integration of stationary batteries for fast charge EV charging stations. *Energies* **2019**, *12*, 24. [CrossRef]
10. Mahfouz, M.M.; Iravani, M.R. Grid-Integration of Battery-Enabled DC Fast Charging Station for Electric Vehicles. *IEEE Trans. Energy Convers.* **2020**, *35*, 375–385. [CrossRef]
11. Vasiladiotis, M.; Rufer, A. A Modular Multiport Power Electronic Transformer With Integrated Split Battery Energy Storage for Versatile Ultrafast EV Charging Stations. *IEEE Trans. Ind. Electron* **2015**, *62*, 3213–3222. [CrossRef]
12. Gjelaj, M.; Hashemi, S.; Traeholt, C.; Andersen, P.B. Grid integration of DC fast-charging stations for EVs by using modular li-ion batteries. *IET Gener. Transm. Distrib.* **2018**, *12*, 4368–4376. [CrossRef]
13. Sbordone, D.; Bertini, I.; Pietra, B.D.; Falvo, M.C.; Genovese, A.; Martirano, L. EV fast charging stations and energy storage technologies: A real implementation in the smart micro grid paradigm. *Electr. Power Syst. Res.* **2015**, *120*, 96–108. [CrossRef]
14. Negarestani, S.; Fotuhi-Firuzabad, M.; Rastegar, M.; Rajabi-Ghahnavieh, A. Optimal Sizing of Storage System in a Fast Charging Station for Plug-in Hybrid Electric Vehicles. *IEEE Trans. Transp. Electrif.* **2016**, *2*, 443–453. [CrossRef]
15. DNV GL. DNVGL-RP-0043 Safety, Operation and Performance of Grid-Connected Energy Storage Systems. *DNV GL*, Recommended Practice Report DNVGL-RP-0043. 2017. Available online: https://rules.dnvgl.com/docs/pdf/DNVGL/RP/2017-09/DNVGL-RP-0043.pdf (accessed on 22 February 2021).
16. Ci, S.; Lin, N.; Wu, D. Reconfigurable Battery Techniques and Systems: A Survey. *IEEE Access* **2016**, *4*, 1175–1189. [CrossRef]
17. Gallardo-Lozano, J.; Romero-Cadaval, E.; Milanes-Montero, M.I.; Guerrero-Martinez, M.A. Battery Equalization Active Methods. *J. Power Sources* **2014**, *246*, 934–949. [CrossRef]
18. Morstyn, T.; Momayyezan, M.; Hredzak, B.; Agelidis, V.G. Distributed Control for State-of-Charge Balancing Between the Modules of a Reconfigurable Battery Energy Storage System. *IEEE Trans. Power Electron.* **2016**, *31*, 7986–7995. [CrossRef]
19. Ci, S.; Zhang, J.; Sharif, H.; Alahmad, M. A Novel Design of Adaptive Reconfigurable Multicell Battery for Power-Aware Embedded Networked Sensing Systems. In Proceedings of the IEEE GLOBECOM 2007—IEEE Global Telecommunications Conference, Washington, DC, USA, 26–30 November 2007; pp. 1043–1047. [CrossRef]
20. Muhammad, S.; Rafique, M.U.; Li, S.; Shao, Z.; Wang, Q.; Liu, X. Reconfigurable Battery Systems: A Survey on Hardware Architecture and Research Challenges. *ACM Trans. Des. Autom. Electron. Syst.* **2019**, *24*, 1–27. [CrossRef]
21. Wei, Z.; Zhao, J.; He, H.; Ding, G.; Cui, H.; Liu, L. Future smart battery and management: Advanced sensing from external to embedded multi-dimensional measurement. *J. Power Sources* **2021**, *489*. [CrossRef]
22. Engelhardt, J.; Gabderakhmanova, T.; Rohde, G.; Marinelli, M. Reconfigurable Stationary Battery with Adaptive Cell Switching for Electric Vehicle Fast-Charging. In Proceedings of the 2020 55th International Universities Power Engineering Conference (UPEC), Turin, Italy, 1–4 September 2020; pp. 1–6. [CrossRef]
23. International Electrotechnical Commission (IEC). *Electric Vehicle Conductive Charging System—Part 23: DC Electric Vehicle Charging Station*; International Standard DS/EN 61851-23:2014/AC:2016; IEC: Geneva, Switzerland, 2016.
24. International Electrotechnical Commission (IEC). *Electric Vehicle Conductive Charging System—Part 24: Digital Communication between a DC EV Charging Station and an Electric Vehicle for Control of DC Charging*; International Standard DS/EN 61851-24:2014; IEC: Geneva, Switzerland, 2014.
25. Gabderakhmanova, T.; Engelhardt, J.; Zepter, J.M.; Sørensen, T.M.; Boesgaard, K.; Ipsen, H.H.; Marinelli, M. Demonstrations of DC Microgrid and Virtual Power Plant Technologies on the Danish Island of Bornholm. In Proceedings of the 2020 55th International Universities Power Engineering Conference (UPEC), Turin, Italy, 1–4 September 2020; pp. 1–6. [CrossRef]
26. Sinopoly Battery. SP-LFP100AHA. Datasheet for SP-LFP100AHA Battery Cell. Available online: http://www.sinopolybattery.com/userfiles/files/SP-LFP100AHA.pdf (accessed on 18 January 2021).
27. Vishay Siliconix. sira20dp. Datasheet for N-Channel 25 V (D-S) MOSFET. Available online: https://www.vishay.com/docs/76212/sira20dp.pdf (accessed on 21 February 2021).
28. *MATLAB*, Version 9.7.0.1190202 (R2019b); The MathWorks Inc.: Natick, MA, USA, 2019.
29. Anseán, D.; García, V.M.; González, M.; Viera, J.C.; Blanco, C.; Antuña, J.L. DC internal resistance during charge: Analysis and study on LiFePO4 batteries. In Proceedings of the 2013 World Electric Vehicle Symposium and Exhibition (EVS27), Barcelona, Spain, 17–20 November 2013; pp. 1–11. [CrossRef]
30. Calearo, L.; Thingvad, A.; Marinelli, M. Validation of a Lumped Battery Model for Electric Vehicle Degradation Studies. Manuscript submitted for publication.
31. Jeong, H.; Lee, H.; Liu, Y.; Kim, K.A. Review of Differential Power Processing Converter Techniques for Photovoltaic Applications. *IEEE Trans. Energy Convers.* **2019**, *34*, 351–360. [CrossRef]
32. Lee, W.; Kim, J.; Lee, J.; Lee, I. Design of an Isolated DC/DC Topology With High Efficiency of Over 97% for EV Fast Chargers. *IEEE Trans. Veh. Technol.* **2019**, *68*, 11725–11737. [CrossRef]
33. Hoffmann, F.; Pereira, T.; Liserre, M. Isolated DC/DC Multimode Converter with Energy Storage Integration for Charging Stations. In Proceedings of the 2020 IEEE Energy Conversion Congress and Exposition (ECCE), Detroit, MI, USA, 11–15 October 2020; pp. 633–640. [CrossRef]

34. Wei, Z.; Meng, S.; Xiong, B.; Ji, D.; Tseng, K.J. Enhanced online model identification and state of charge estimation for lithium-ion battery with a FBCRLS based observer. *Appl. Energy* **2016**, *181*, 332–341. [CrossRef]
35. Fotouhi, A.; Auger, D.J.; Propp, K.; Longo, S.; Wild, M. A review on electric vehicle battery modelling: From Lithium-ion toward Lithium–Sulphur. *Renew. Sustain. Energy Rev.* **2016**, *56*, 1008–1021. [CrossRef]